Manuscript under review at Nature Communications. Non-peer reviewed preprint for EarthArXiv

Ancient subducted oceans controlling the positioning of deep mantle plumes

Philip J. Heron[1], Juliane Dannberg[2,3], Rene Gassmöller[2,3], Grace E. Shephard[4], J. van Hunen[1] & R. N. Pysklywec[5]

[1] *Durham University, Dept of Earth Sciences, Durham, DH1 3LE, United Kingdom*

[2] *University of California Davis, Davis, CA 95616-5294, United States*

[3] *University of Florida, Gainesville, FL 32611, United States*

[4] *Center for Earth Evolution and Dynamics (CEED), Department of Geosciences, University of Oslo, Norway*

[5] *University of Toronto, Dept of Earth Sciences, Toronto ON, Canada*

Seismic imaging of the Earth's interior reveals plumes originating from relatively hot regions of the lower mantle, surrounded by cooler material thought to be remnants of ancient subducted oceans. Based largely on geophysical data, two opposing hypotheses dominate the discussion on dynamics at the base of mantle: the large hot anomalies are thermo-chemical in nature; or, alternatively, they are purely thermal plume clusters. In previous modelling studies, deep chemical heterogenities have been argued to be essential in developing appropriate present-day plume positions. Here, we quantify how the chemical composition of large, hot regions in the deep mantle influences the location of rising mantle plumes using numerical 3-D global mantle convection models constrained by 410 million years of palaeo-ocean evolution. For the first time, we show that purely thermal convection can reproduce the observed

positions of present-day hotspots. By demonstrating that a lower mantle without large-scale chemical heterogeneities can generate appropriate global dynamics, we illustrate the power of sinking ocean plates to stir mantle flow and control the thermal evolution of the mantle. Because our models with a thermo-chemical anomaly reproduce the observed hotspot positions equally well, we posit that the deep hot anomalies in the mantle are purely passive in global dynamics - regardless of their (thermal or chemical) origin.

Large structures of low seismic velocities (the Large Low Shear Velocity Provinces, or LLSVPs) observed in the lower mantle in seismic tomography studies and interpreted as regions of elevated temperatures, appear to play a defining role in the origins and positioning of mantle plumes[1–4]. Although the fundamentals of composition and origin of LLSVPs are still being debated[5–8], there is growing agreement[9] that plumes may form in some way from these regions (Figure 1). The formation of plumes can influence supercontinent dispersal, leading to a further repositioning of subduction zones and a change in mantle flow[10].

The nature of LLSVPs has been at the centre of plume generation discussions for over a decade[2,6,12]. Geochemical data from surface melts indicate the presence of chemical mantle reservoirs[13–22], with hotspot-derived melts associated with plumes consistently showing a different mantle source composition than mid-ocean ridge basalts. Recent evidence suggests that spatial geochemical patterns at oceanic islands reflect preferential sampling of a distinct source of deep mantle material originating from the LLSVPs[23–25]. These observations have led to the idea that the LLSVPs may be ‘thermo-chemical’ piles of material with a different composition than the average

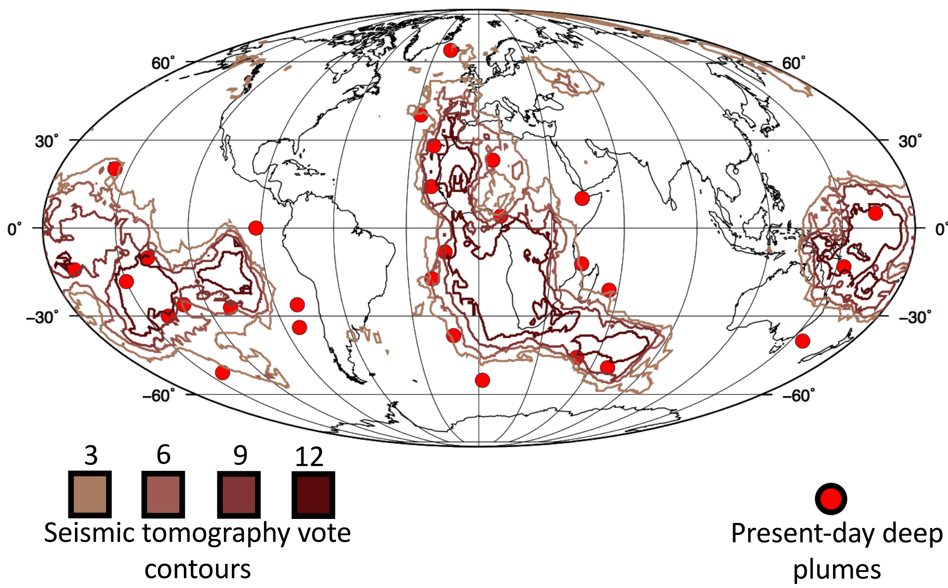

Figure 1: Present-day mantle features. Position of low velocity provinces (LLSVPs) at 2800 km depth alongside present-day deep mantle plume and hotspot locations[1,4] (SI Table S.1). The low velocity regions are contours where 3, 6, 9, and 12 (out of 14) seismic tomography models agree that there are slow anomalies[11].

mantle.

A divided view is presented by seismology. The two deep anomalies have been characterized by higher than average densities through early tomographic normal mode data and the anti-correlation of bulk sound and shear wave anomalies[26–30]. More recent analysis using tidal tomography has also inferred structures of increased density in the lower mantle[31]. However, work using Stoneley mode data offered an opposing view which indicated the potential for lighter material[7]. Compositional heterogeneities and/or a phase change to post-perovskite could both fit seismic observations in the lowermost mantle[32,33] – though, the possibility that LLSVPs are purely thermal anomalies has also been put forward[34].

Previous geodynamic modelling studies have indicated that a thermo-chemical nature of the deep mantle material is essential in producing appropriate present-day plume positions[35–37]. However, the rheological nature of LLSVPs, and their role in mantle dynamics, is still being debated[6,8,9,12,38,39]. Important open questions remain: Are LLSVPs thermal plume clusters or dense, stable thermo-chemical piles, or a mixture of the two?; Have LLSVPs been present and stable for most of the Earth's history?; and do they control the location of rising plumes? A key component to answering these questions lies in understanding the mechanisms that cause plumes to rise in the locations where hotspots are observed on Earth today.

To study mantle dynamics, we use 3-D thermo-chemical global mantle convection experiments that take into account palaeo-subduction history from 410 Ma to the present day[40] (which incorporates plate reconstructions models of the Paleozoic[41] and Mesozoic-Cenozoic[42]). We then compare the results at the end of the model run to observations of LLSVP shape[3,4,11] and plume positions[1,4]. By applying different subduction histories as a time-dependent boundary condition to our models [e.g.,6,35–37,43–48], we gain insights on the role of subducted slabs in shaping the LLSVPs and triggering the ascent of mantle plumes. In addition, we systematically vary the thickness of compositional heterogeneity in the lowermost mantle, thereby controlling the dynamics of the hot regions that represent the LLSVPs. This allows us to evaluate which of the proposed end-member scenarios – an anomaly that is purely thermal or one that is thermo-chemical – is supported by the observations.

A key innovation in our approach compared to previous studies is that we incorporate subduction history encompassing the formation and breakup of the supercontinent Pangea. The life-cycle of a supercontinent has a dramatic impact on mantle dynamics[49], and we show that the subduction history affects plume and LLSVP formation on different time scales. Here, our models discover the mantle circulation dynamics that connect past plate motions and ocean island volcanism. We show that the two opposing hypotheses – plume clusters and thermo-chemical piles – are both able to reproduce the observed positions of present-day hotspots equally well, highlighting the importance of ancient subducted oceans in stirring the convecting mantle.

Results

Mantle dynamics. We computed a suite of geodynamic models with varying amounts of chemical heterogeneity in the mantle in order to investigate a wide range of lower-mantle convection regimes: plume clusters, stable thermo-chemical piles, and metastable piles. Our models begin from an initial condition at 410 Ma (Figure 2 and Table 1) that assumes a realistic average mantle temperature and composition. The initial mantle temperature is laterally homogeneous, following an adiabatic profile with thermal boundary layers at the top and bottom[50], and any anomalous, dense material is initially emplaced as a uniform layer at the core-mantle boundary. We vary the initial thickness of this layer between 0 km (purely thermal model) and 300 km for different model runs (SI Table S.2; Model0, Model100, Model150, Model200, Model250, and Model300). In Model200, the subduction pattern during the formation and dispersal of the supercontinent Pangea shapes the hot thermo-chemical material into two distinct regions in roughly the same locations as the observed LLSVPs (e.g., Figure 3). We herein refer to thermo-chemical piles from the numerical models as 'TCPs' and reserve the 'LLSVPs' for the seismically imaged structures to which TCPs are compared.

All simulations where the initial dense layer is at least 150 km thick produce two distinct thermo-chemical piles (TCP, Figure 4). Model100 results in all the thermo-chemical material being entrained into the mantle during the simulation (SI Figure S.2), and Model0 features thermal plume clusters. Correlating the modelled African TCP with the shape of the African LLSVP (as given by the agreement of 8 seismic tomography studies), we find that Model200 produces the best fit (SI Table S.2). The Pacific thermo-chemical pile also forms in the correct hemisphere in Model200, but the agreement with seismic tomography[11] is generally not as good as in the African hemisphere. The modelled Pacific pile extends further north and south than the slow anomalies in tomography studies, and it is missing the western limb when compared with the LLSVP outline

(Figure 3h).

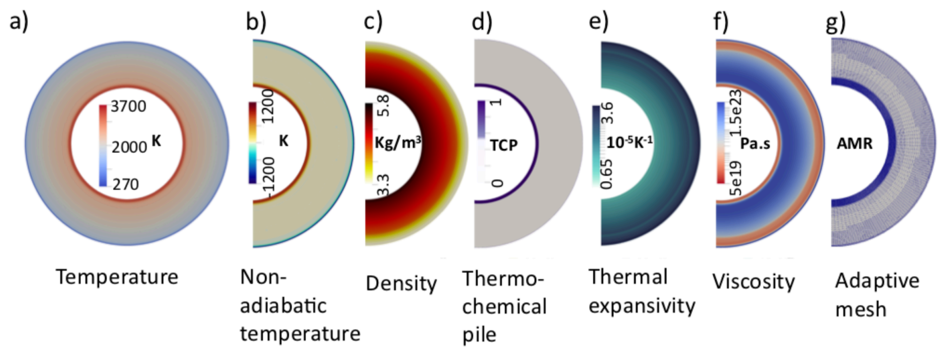

Figure 2: Initial conditions of the models (at 0 Myr/410 Ma), showing cross-sectional views of a) temperature, b) non-adiabatic (excess) temperature, c) density, d) initial thermo-chemical pile thickness (200 km in Model200 shown here), e) variable thermal expansivity, f) viscosity, g) the initial adaptive mesh.

Figure 5a shows the mantle under the northern Atlantic and Europe, indicating the excess temperature anomalies for upwelling plumes (red) and downwelling material (blue) for Model200. Comparing this model output at the equator to seismic tomography studies[3] shows a number of similarities. Under Africa, our model TCP matches the shape of the LLSVP outline well, highlighting the steep western side[55] and angled eastern flank (A and B, Figure 5b). In the Pacific hemisphere, our Model200 produces plume positions in the Galapagos (C, Figure 5b) as well as a TCP in the eastern part of the Pacific LLSVP (D, Figure 5b). However, our model misses the western flank of the Pacific LLSVP across the equator (E, Figure 5b) as shown in Figure 3h. Further direct comparisons with another seismic study[4] are given in SI Figure S.1.

Present-day plume analysis. Direct comparison between tomography slices (Figure 5b-c,

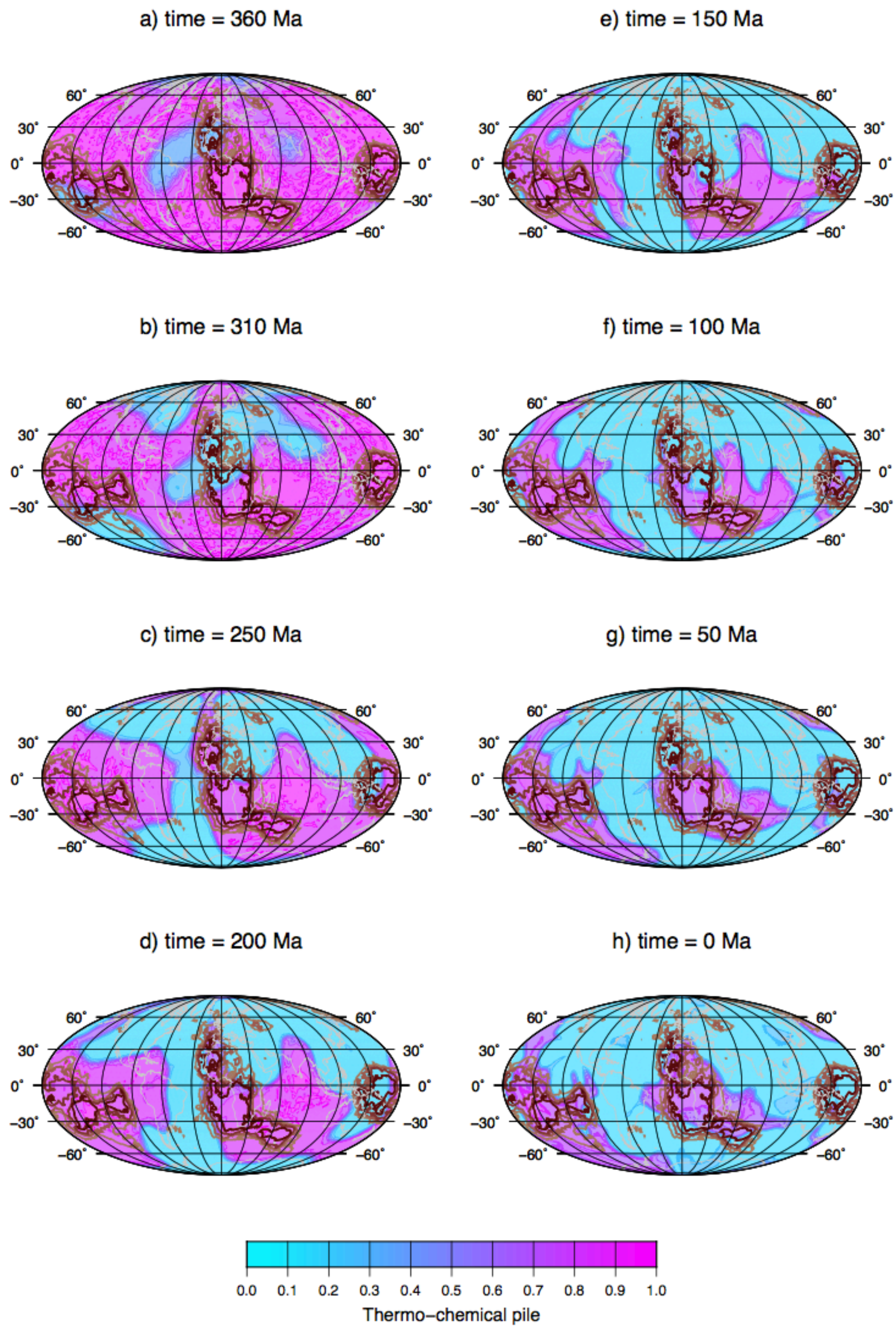

Figure 3: Evolution of chemical heterogeneities in Model200 from 410 Ma to present day. The snapshots (a)-(h) show the proportion of anomalous, dense material in a spherical slice at 2800 km depth, illustrating how the material evolves from a layer with uniform thickness into a thermo-chemical pile. Brown contours indicate low seismic velocity anomalies as in Figure 1.

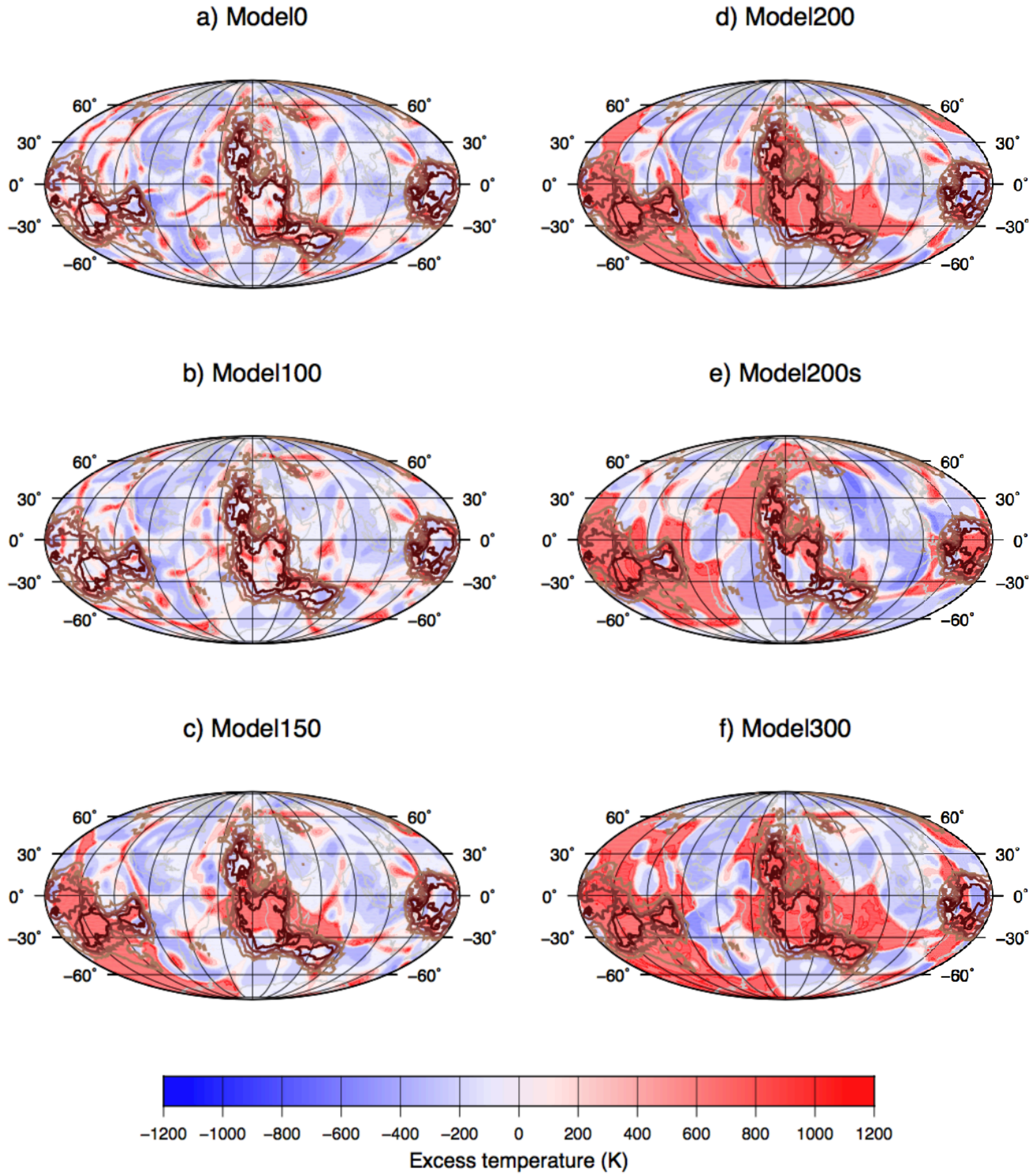

Figure 4: Differences in core-mantle boundary temperature and dynamics between models with varying amount of chemical heterogeneity. Present-day (0 Ma) excess temperature in 2800 km depth for a) Model0, b) Model100, c) Model150, d) Model200, e) Model200s, and f) Model300.

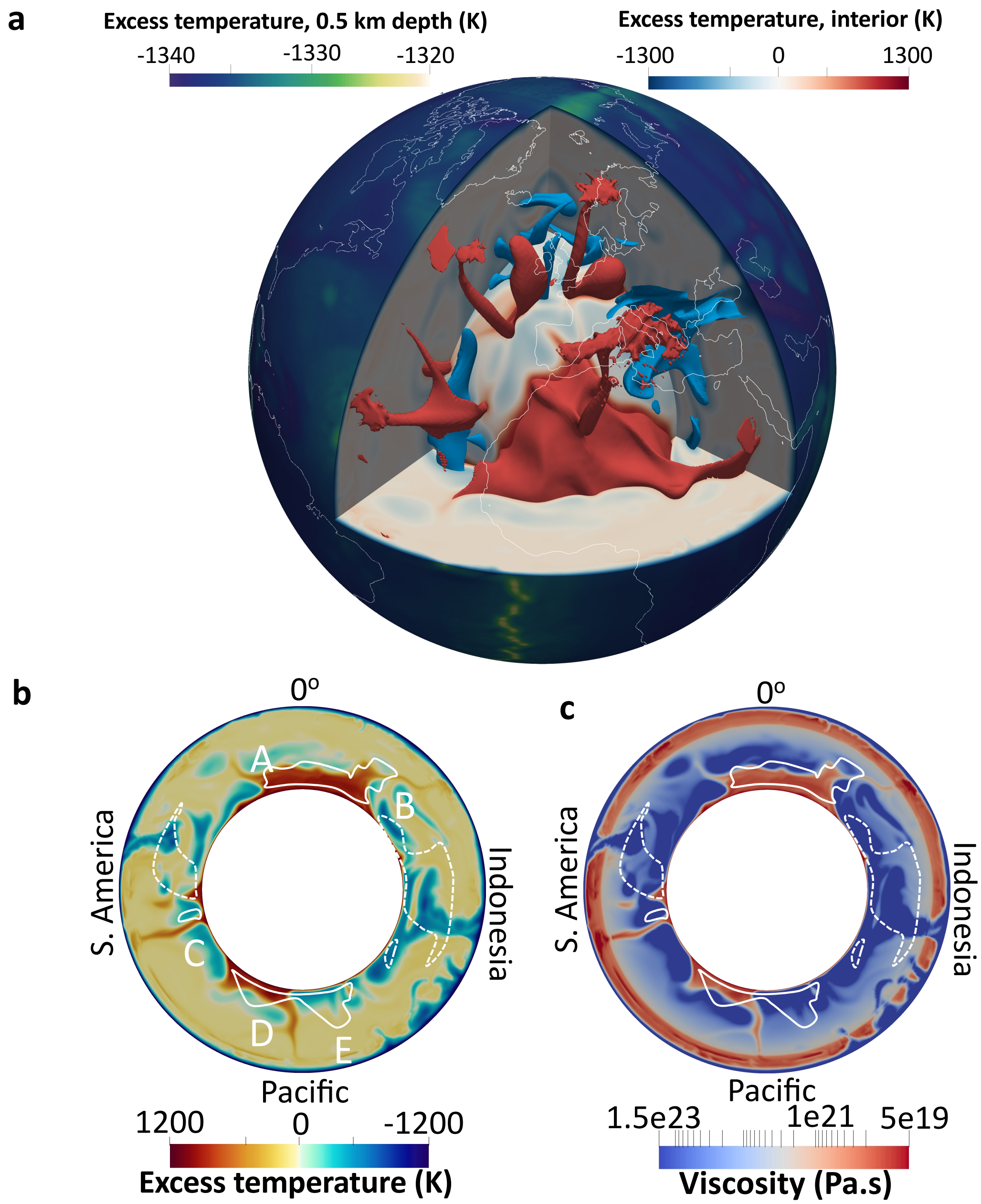

Figure 5: Global mantle dynamics and temperature compared with seismic models. a) A view into the mantle beneath the northern Atlantic and Europe for Model200. Excess mantle temperature anomaly contoured surfaces are given for warm (300 K, red) and cold (-500 K, blue) regions. b) Excess temperature slice at the equator, and the corresponding viscosity distribution (c), with the outline of where four seismic tomography studies agree that there is a shear velocity anomaly[3] shown by white solid (slow) and dashed (fast) lines. Key: A: steep western side of the African LLSVP; B: angled eastern flank of the African LLSVP; C: Galapagos plume position; D:

Table 1: Material parameters.

Symbol	Variable	Value
η	Dynamic viscosity	literature[51]
ρ	Density	PerpleX[52–54]
g	Gravitational acceleration	9.81 $m.s^{-1}$
C_p	Specific heat capacity	PerpleX[52–54]
k	Thermal conductivity	4.7 $W.m^{-1}.K^{-1}$
H	Radiogenic heat production	6×10^{-12} $W.kg^{-1}$
α	Thermal expansivity	PerpleX[52–54]

SI Figure S.1) can give a first order interpretation of how well the models reproduce present-day mantle dynamics. However, a better representation of model accuracy is to compare the difference between a present-day deep mantle plume and hotspot database[1,4] (SI Table S.1) and the position of hot thermal anomalies in our models.

Figure 6a illustrates the position of upwellings of Model200 at 700 km depth (green) alongside the present-day plume and hotspot database[1,4] (red). The plume positions in our model do not appear to be randomly distributed, with upwellings forming close to the upwards projected margins of the LLSVPs in the African domain. In the Pacific, a number of Model200 plumes form close to edges of the LLSVPs. Interestingly, this occurs in the western limb of the Pacific LLSVP even though there is no modelled thermo-chemical pile in that position (Figure 3h). A number of Model200 plumes form within 1000 km of the Azores, Afar, Comores, St Helena, San Felix, Galapagos, Easter, and Pitcairn plumes (markers G to N in Fig 6a, respectively). Furthermore, a deep mantle plume is positioned at the Louisiade site (marker O, Figure 6a) where a previous study[4] had imaged a plume despite no corresponding surface hotspot.

Figure 6a also shows the positioning of plumes generated from a model that does not feature any thermo-chemical piles (Model0). The blue circles show plume positions at 700 km depth for a purely thermal mantle convection model without chemical heterogeneities. There is a strong similarity between the blue and green plume positions despite different lowermost mantle structure. Indeed, more than half of the Model0 plumes form within a radius of 900 km from the Model200 plumes (SI Figure S.4), indicating that the thermo-chemical pile is not the driving force in plume positioning.

To test how statistically relevant our results are, we look at the distance each plume in our model forms away (at 700 km depth) from the nearest present-day hotspot in the database[1,4] (assuming sub-vertical ascent of the plume in the upper mantle). Figure 7 shows the percentage of database hotspots as a function of their distance from the nearest plume in Model0 (no thermo-chemical pile), Model200 (200 km initial thickness), and Model300 (300 km initial thickness). A lower distance for the database plume percentage indicates that there is a better fit between modeled plume positions and the location of hotspots in the database (the model is performing well). For instance, Model300 shows that all of the model plumes fall within 4000 km of a database plume. However, less than 48% of the database plumes fall within 1500 km of a Model300 plume. In comparison, Model0 and Model200 perform much better, with 51% and 59% of the database

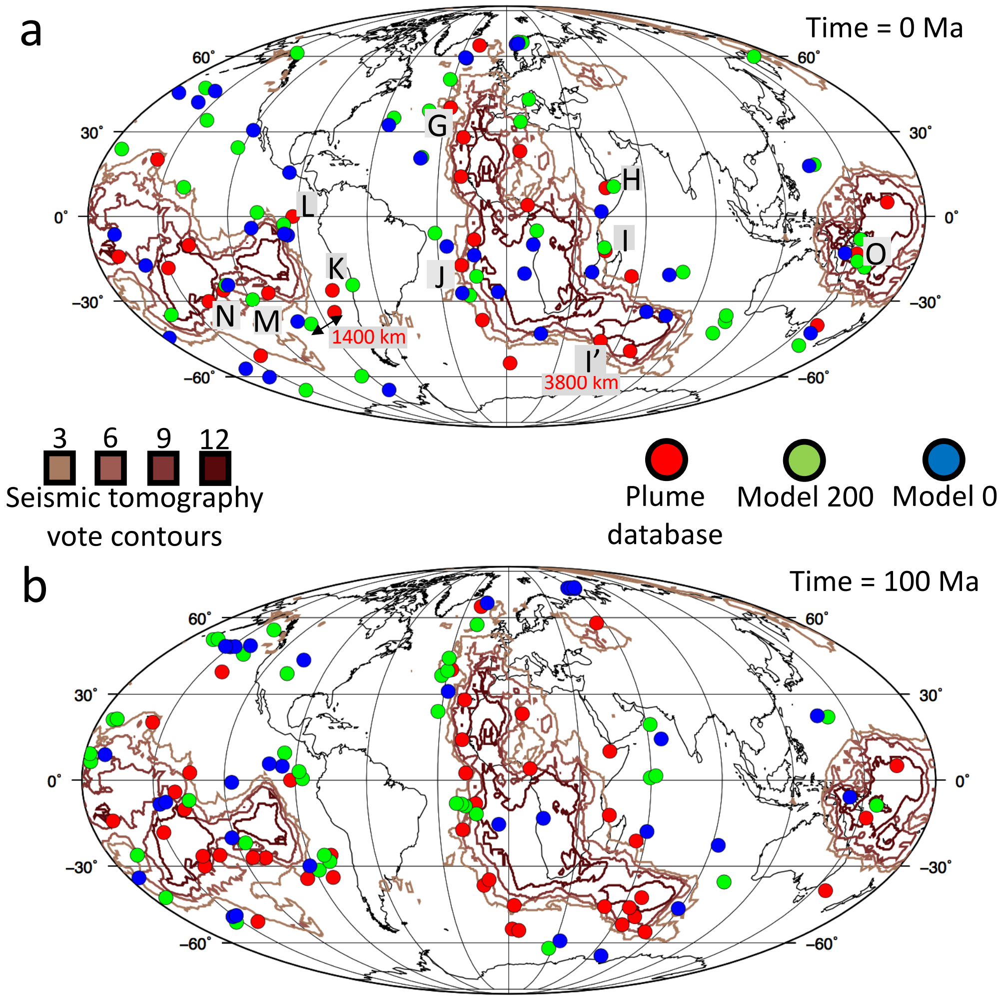

Figure 6: A number of model upwellings form close to the edges of LLSVPs and reach close to the surface near observed present-day hotspots. a) Plume positions at 0 Ma for Model200 (green), Model0 (blue), and the hotspot database[1,4] (red) as given in SI Table S.1. b) Plume positions at 100 Ma for the above models alongside a large igneous province database for 300 – 100 Ma (red) as given in SI Table S.3[2]. Plume key: G: Azores; H: Afar; I: Comores; J: St Helena; K: San Felix; L: Galapagos; M: Easter; N: Pitcairn; O: Louisiade. Two markers are given to indicate plume distances: 1400 km is shown between the Juan Fernandez plume and the nearest Model200 output; and 3800 km between I and I' (representing the largest distance between a database plume and a Model200 output).

plumes, respectively, falling within 1500 km or less from a model plume.

Figure 7 also shows 10,000 randomly generated sets of 39 plume positions (grey lines). The percentile distribution of these artificially generated points is given by the areas shaded in grey and shows what percentage of the random models falls within a specific distance. In the case of the lightest grey area, less than 15% of the random models have smaller distances to the database plumes than shown. The profiles of Model0 and Model200 follows this 15% line closely, indicating that these models perform better than 85% of the randomly generated results.

Model200s applies a 410 Myr plate reconstruction that uses an extended version of Seton et al.[56] 250 Ma to 90 Ma surface velocities for 410 Ma to 250 Ma, then repeats from 250 Ma until present-day[45] (0 Ma) using the rheological setup of Model200. In other words, the velocity boundary conditions applied in the first 160 Myr of model evolution probably do not represent past plate motions well. In applying these surface velocities, we can test the relative importance of supercontinent formation (e.g., 410 Ma to 250 Ma) in developing plume positions. Figure 7 indicates that Model200s performs as well as Model200 for the majority of database plumes. However, the surface velocities from the more recent global model of Matthews et al.[40] that incorporate supercontinent formation do have an impact on the shape of the thermo-chemical piles in our models. Figure 4 indicates that applying appropriate surface velocities for the final 250 Myr (e.g., Model200s) is not enough time to mould the thermo-chemical pile under Africa into place (or, indeed, that piles are required to be already in position at that time). Although there is good agreement between the TCP and the Pacific LLSVP, the African thermo-chemical pile appears to be at a higher latitude when compared to a model that has undergone supercontinent formation and dispersal surface velocities (e.g., Model200).

Discussion

In contrast to previous studies[35–37], we reproduce present-day plume positions both in models that begin (at 410 Ma) with and without thermo-chemical piles (Figure 6a). This result reveals that LLSVPs are a relatively passive feature of mantle dynamics (as shown in Figure 8), and that ancient subducted ocean plates, rather than chemical heterogeneity, are the dominant factor driving global mantle circulation.

The work presented here has wider implications on mantle dynamics. The proximity of ancient large igneous provinces (LIPs) to the edges of present-day LLSVPs has often been cited as a reason why deep mantle heterogeneities may be dynamically stable over 500 Myr time-frames[2,57]. By analysing the upwelling locations for Model200 and Model0 during the Cretaceous (100 million years in the past), the position of plumes still often occurs near the margins of present-day LLSVPs (Figure 6b). This is significant given that our thermo-chemical piles are not fixed over time (Figure 3 and 8) or not present at all (e.g., Model0). Consequently, LLSVPs do not need to be laterally fixed on supercontinent timescales[2,57] to produce appropriate plume positions in the present or (potentially) in the past. Instead, the relative stability of subduction zones over the last 100 million years may be the crucial factor for fixing the proximity of past plumes to present-day LLSVP margins. Our models indicate a decoupling of mantle timescales for plume positions (short

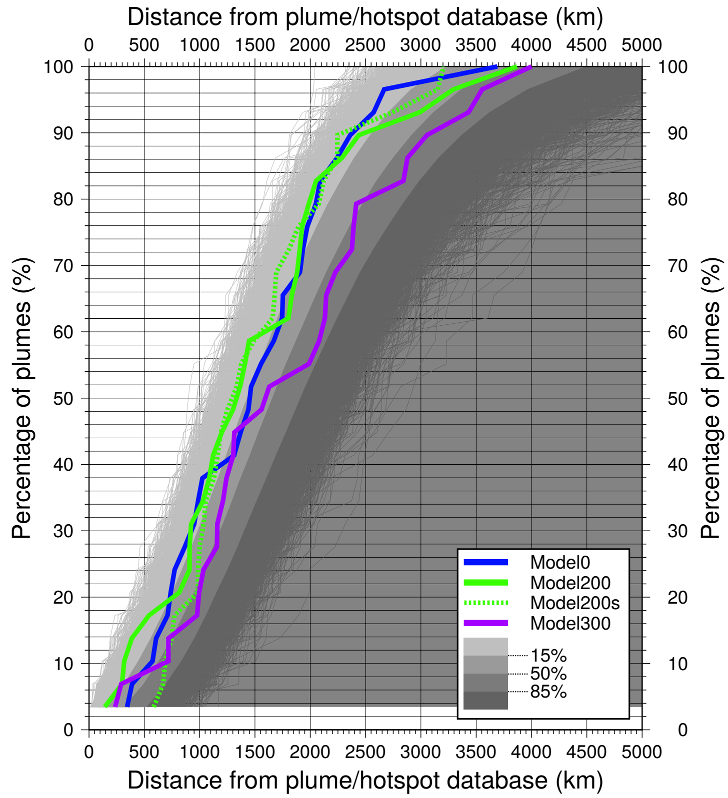

Figure 7: Analysis of model plume positions at 0 Ma as a function of distance away from the nearest present-day hotspot[1,4]. For any distance given on the x-axis, the blue, green and purple lines show the percentage of model plumes that reach the surface closer to an observed present-day hotspot than this distance (for details on the analysis, see the Methods section). The purely thermal Model0 generates 37 plumes; Model200 (starting from a basal layer of dense material with 200 km thickness) features 39 plumes; and Model300 (with a 300-km basal layer) produces 32 plumes. Model200s utilizes 410 Myr of palaeo-subduction history using a modified reconstruction history (see Table S.2) and produces 29 plumes. Grey lines show 10,000 sets of 39 artificially generated random plume positions. The shaded grey areas indicate the percentile distance distribution 15%, 50%, and 85% of the 10,000 random models (see also SI Figure S.3). For most distances, Model0 and Model200 perform better than 85% of the random model runs.

scale) and LLSVP dynamics (longer scale), controlled by the plate motion history.

Model200s further indicates a decoupling in timescales between the development of plumes and the positioning of LLSVPs beneath Africa and the Pacific. For instance, by only running appropriate plate reconstruction history for the past 250 Ma (instead of 410 Ma in Model200), Model200s does not produce a thermo-chemical pile in the southern hemisphere under Africa (Figure 4e). However, in analysis of the plume positions, Model200s performs as well as Model200 (Figure 7). Although the past 250 Myr of subduction history is sufficient to develop a mantle flow with appropriate present-day upwellings, it may take longer for dense thermo-chemical piles to be moulded into position by subduction.

Although we highlight that LLSVPs do not need to be spatially fixed over supercontinent timescales, our models do not, and cannot, rule out an LLSVP being either purely thermal anomalies (Model0), (meta)stable chemical piles of dense material (Model200), or a combination of the two (Model100) (Figure 9). In contrast to our work, previous studies found that a thermo-chemical simulation, rather than a purely thermal model, is required to produce appropriate plume positions for present-day hotspots[35–37]. However, Davies et al.[6] previously showed that observed lower mantle shear wave velocity anomalies do not require large-scale chemical piles to obtain appropriate LLSVP dynamics. Although Davies et al.[6] did not conduct a formal plume analysis as given in our study, they did find that purely thermal LLSVPs (e.g., iso-chemical) could reconcile observed shear wave velocity anomalies and gradients. The work presented in our study highlights that purely thermal geodynamic models can not only produce seismological features of the deep mantle[e.g.,6], but also reproduce mantle dynamics in the form of plume locations (Figure 6a).

Our work implies that the decoupling of plume generation and large-scale mantle flow timescales makes it difficult to unravel the composition of LLSVPs from numerical models alone (Figure 9). As a result, we posit that the key to understanding the seismic anomalies in the present-day deep mantle can only come from direct sampling, and therefore additional geochemical data and seismologic observations. However, we suggest that the meta-stability of these structures can be cogent with observed mantle dynamics (Figure 5), regardless of whether they are chemically distinct or purely thermal (Figure 6), and signal that the deep mantle may evolve as significantly as our tectonic surface (Figure 3 and 8).

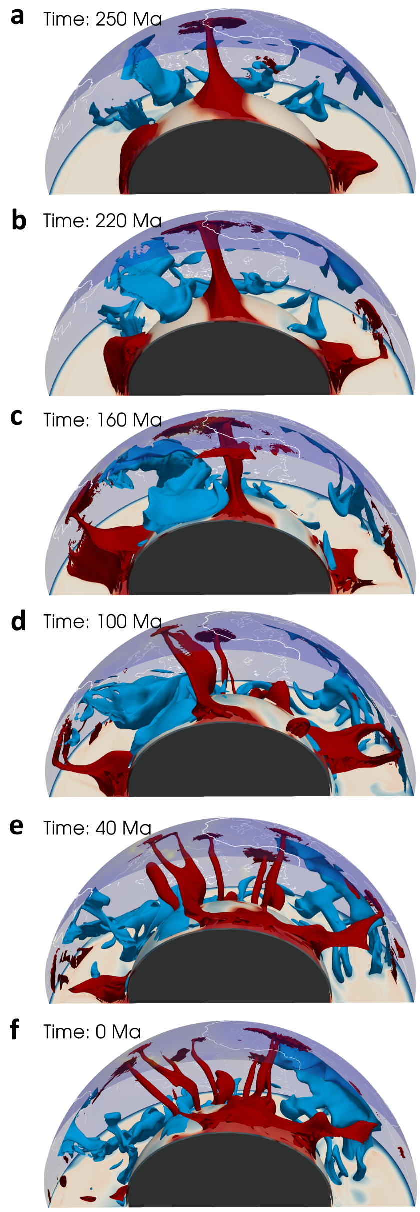

Figure 8: Thermo-chemical piles are passive in mantle dynamics. Evolution of the hot and cold anomalies under the African northern hemisphere from 250 Ma (a) to present-day (f) for Model200. Slice contours as Figure 5.

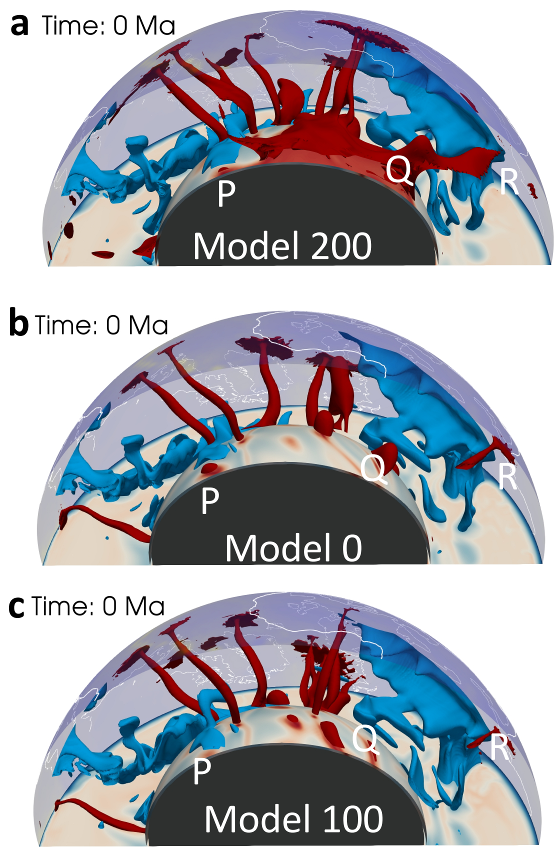

Figure 9: Models with different amount of chemical heterogeneity can produce appropriate plume dynamics. Present-day snapshot of the hot and cold anomalies under the African northern hemisphere for (a) Model200, (b) Model0, and (c) Model100. Slice contours as Figure 5. Markers P, Q, and R indicate equatorial plumes that could be linked to present-day hotspots St Helena, Comores, and Afar, respectively.

Methods

Model setup. Computations were done using the ASPECT code[58,59]. ASPECT solves the following set of equations for compressible convection in the Earth's mantle, describing the mass, force and energy balance (taking into account adiabatic heating, shear heating and radiogenic heat production), and the transport of chemical composition:

$$-\nabla \cdot (2\eta\dot{\varepsilon}) + \nabla p = \rho \mathbf{g}, \tag{1}$$

$$\nabla \cdot (\rho \mathbf{u}) = 0, \tag{2}$$

$$\rho C_p \left(\frac{\partial T}{\partial t} + \mathbf{u} \cdot \nabla T \right) - \nabla \cdot k \nabla T = \rho H + 2\eta(\dot{\varepsilon} : \dot{\varepsilon}) + \alpha T \left(\mathbf{u} \cdot \nabla p \right), \tag{3}$$

$$\frac{\partial C}{\partial t} + \mathbf{u} \cdot \nabla C = 0. \tag{4}$$

The equations are solved for velocity $\mathbf{u}$, pressure p, temperature T and chemical composition C. η is the viscosity, $\dot{\varepsilon} = \frac{1}{2}(\nabla \mathbf{u} + \nabla \mathbf{u}^T) - \frac{1}{3}(\nabla \cdot \mathbf{u})\mathbf{1}$ is the deviatoric strain rate, $\mathbf{g}$ is the gravitational acceleration, ρ is the density, C_p is the specific heat capacity (at constant pressure), k is the thermal conductivity, H is the radiogenic heat production, and α is the thermal expansivity.

We use the global model setup[59] employed in a previous study[50], except for the following modifications:

- our plate reconstruction[40], which provides velocity boundary conditions at the surface of the model, extends back in time 410 million years,
- we vary the amount of dense recycled oceanic crust material (e.g., the thermo-chemical pile) that is present in the mantle, changing the thickness of the layer at the core-mantle boundary

where the material is distributed at the model start between 0 to 300 km (see SI Table S.2),

- we fix the core-mantle boundary temperature to 3700 K, corresponding to a buoyancy number $B = \frac{\Delta\rho}{\alpha\rho\Delta T} = 1.9$ (where $\Delta\rho$ is the density contrast between the anomalously dense material and the average mantle composition and ΔT is the difference between the actual core-mantle boundary temperature and the adiabatic profile) at a depth of 2500 km.

As in a previous study[50], we assume an average mantle composition of 82% harzburgite and 18% recycled oceanic crust[54] and compute the material properties ρ, α and C_p using Perple_X[52] and a mineral physics database[53]. Accordingly, all material properties include the effects of phase transitions, with with thermal expansivity and specific heat approximating the corresponding latent heat release[60]. All model parameters are given in SI Table 1, and the initial radial profiles of temperature- and depth-dependent material properties are plotted in Figure 2.

Analysis of plume positions and thermo-chemical pile shape. To determine the locations of mantle plumes in our models, we define a plume as a positive temperature anomaly of at least 300 K excess temperature at a depth of 700 km. This depth was chosen in order to capture a first-order location of the conduit and to avoid complications with plume head and upper mantle entrainment complexities. These regions are then collated and spatially averaged into one data point for each plume. Table S.1 and Fig 1 show the hotspot catalogue[1,4] we use as a comparison for the output of our geodynamic models. We quantify how well each model output fits this database of present-day hotspots (as illustrated in Figures 7, S.3, S.4 and S.7) by using the following statistical method for comparing two sets of points:

We calculate the distance d between the model plumes and the hotspots in the database using the Spherical Law of Cosines:

$$d = \arccos(\sin(\phi_{db})\sin(\phi_m) + (\cos(\phi_{db})\cos(\phi_m)\cos(\lambda_m - \lambda_{db})))r_e \quad (5)$$

where ϕ and λ are the latitude and longitude, respectively, of the plume location in the model (m) and the position of the closest hotspot in the database (db), and r_e is the radius of the Earth. The results are given in Fig 7, showing the percentage of the 29 hotspots in the database that are in a given distance from any of the modeled plumes.

To quantify how well each model fits the hotspot database, we use Equation 5 to compute the same statistics for 10,000 random plume positions, generated from a set of 39 random latitudes ϕ_m and longitudes λ_m. Each result of a random run is plotted as a grey line in Fig 7. These random runs allow us to compute percentiles (shown as shaded grey areas in Fig 7), indicating if the fit of a given model is better than, for example, the 15%, 50%, or 85% of the best random sets of plume positions. Here, the 50% percentile is equivalent to the average fit expected for a random plume distribution, and the 15% and 85% percentiles indicate approximately one standard deviation of this distribution. We generate the percentiles in Fig 7 through analysing histograms, with each histogram corresponding to a horizontal slice through the 10,000 random plume models in the diagram. In other words: To generate a histograms for a given cumulative fraction of hotspots x, we pick the x database hotspots that are closest to any plume in a given random plume distribution. Each of the 10,000 data points in each of the histograms shows the maximum distance between any of these hotspots and the closest model plume. For example, a histogram showing the maximum distance of the 52% database hospots that are closest to plumes in each of the 10,000 random models is given in Fig S.3. This distribution allows us to determine the cutoff distance for the 15%, 50%, and 85% of the best random models. To generate a percentile distribution profile, as given by the shaded areas in Fig 7, these cutoff distances are produced for all the cumulative plume percentages (e.g., from 1 out of 29 plumes (3%) to 29 out of 29 (100%)).

To test the robustness of our findings we also computed a higher-resolution convection simulation with the same setup as Model200. Compared to Model200, we increased the resolution by a factor of two, reduced the time step size by a factor of 2, and reduced the nonlinear solver tolerance from 10^{-3} to 10^{-5}. The results of this Model200hr are shown in Figures S.5 to S.7. The position of the thermo-chemical piles on an equatorial slice are similar in both models, but the higher resolution model allows for more accurate (lower) thermal diffusion, reducing the thickness of cold downwellings, as shown in Figure S.5.

For the same reason, we also find that in the upper mantle, the upwelling plumes are thinner and not as hot in the higher resolution model. To generate a similar number of model plumes for the statistical analysis as in the other models, we define plumes as regions with an excess temperature of at least 200 K at 700 km depth (rather than 300 K as in Model200). This classification produces 29 Model200hr plumes in positions shown by the white circles in Figure S.6. The plume positions are not identical to the lower resolution model (Figure S.6a) and the thermo-chemical pile covers more of the core-mantle boundary than in Model200 (Figure S.6b). However, Figure S.7 does show that the results are robust with regards to the plume positioning consistently performing better than the random models.

Vote maps[11] are a simple tool that counts how many tomographic models detect the same structure in a given location; a high "vote" count indicates agreement across the given suite of models. In this study, the vote maps detect slow anomalous wavespeeds in order to detect the edges of the LLSVPs. The vote maps were constructed with 14 tomography models (7 P-wave and 7 S-wave) and methodology used in the construction of the vote maps are listed in a previous study[11]. The correlation between the thermo-chemical pile shape and present-day LLSVP outline under Africa, as outlined in Table S.2, is calculated by the correlation between the area bound by the 0.55 thermo-chemical ratio in the model and the 8 vote contour from seismic data[11].

The correlation coefficient is given as

$$r = \frac{\sum\sum(A-\overline{A})(B-\overline{B}))}{\sqrt{\left(\sum\sum(A-\overline{A})^2)(\sum\sum(B-\overline{B})^2\right)}}, \tag{6}$$

where A is the model area and B is the vote map area.

Code availability The modelling code we used is open source and freely available online under the terms of the GNU General Public License at https://github.com/geodynamics/aspect. For our study, we have used version 2.0.0-pre (commit 572f967).

Data availability All input files that are required to reproduce our results are available online at https://github.com/jdannberg/paper-plume-positions-data.

References

1. Steinberger, B. Plumes in a convecting mantle: Models and observations for individual hotspots. *Journal of Geophysical Research: Solid Earth* **105**, 11127–11152 (2000). URL http://dx.doi.org/10.1029/1999JB900398.

2. Torsvik, T. H., Smethurst, M. A., Burke, K. & Steinberger, B. Large igneous provinces generated from the margins of the large low-velocity provinces in the deep mantle. *Geophysical Journal International* **167**, 1447–1460 (2006). URL http://dx.doi.org/10.1111/j.1365-246X.2006.03158.x.

3. Cottaar, S. & Lekic, V. Morphology of seismically slow lower-mantle structures. *Geophysical Journal International* **207**, 1122–1136 (2016). URL http://dx.doi.org/10.1093/gji/ggw324.

4. French, S. W. & Romanowicz, B. Broad plumes rooted at the base of the earth's mantle beneath major hotspots. *Nature* **525**, 95–99 (2015). URL http://dx.doi.org/10.1038/nature14876.

5. Deschamps, F., Cobden, L. & Tackley, P. J. The primitive nature of large low shear-wave velocity provinces. *Earth and Planetary Science Letters* **349-350**, 198–208 (2012). URL http://dx.doi.org/10.1016/j.epsl.2012.07.012.

6. Davies, D. R. *et al.* Reconciling dynamic and seismic models of earth's lower mantle: The dominant role of thermal heterogeneity. *Earth and Planetary Science Letters* **353-354**, 253–

269 (2012). URL http://dx.doi.org/10.1016/j.epsl.2012.08.016.

7. Koelemeijer, P., Deuss, A. & Ritsema, J. Density structure of earth's lowermost mantle from stoneley mode splitting observations. *Nature Communications* **8**, 15241 (2017). URL http://dx.doi.org/10.1038/ncomms15241.

8. Zaroli, C., Koelemeijer, P. & Lambotte, S. Toward seeing the earth's interior through unbiased tomographic lenses. *Geophysical Research Letters* **44**, 11,399–11,408 (2017). URL https://agupubs.onlinelibrary.wiley.com/doi/abs/10.1002/2017GL074996. https://agupubs.onlinelibrary.wiley.com/doi/pdf/10.1002/2017GL074996.

9. Garnero, E. J., McNamara, A. K. & Shim, S.-H. Continent-sized anomalous zones with low seismic velocity at the base of earth's mantle. *Nature Geoscience* **9**, 481–489 (2016). URL http://dx.doi.org/10.1038/ngeo2733.

10. van Hinsbergen, D. J. J., Steinberger, B., Doubrovine, P. V. & Gassmöller, R. Acceleration and deceleration of india-asia convergence since the cretaceous: Roles of mantle plumes and continental collision. *Journal of Geophysical Research* **116** (2011). URL http://dx.doi.org/10.1029/2010JB008051.

11. Shephard, G. E., Matthews, K. J., Hosseini, K. & Domeier, M. On the consistency of seismically imaged lower mantle slabs. *Scientific Reports* **7** (2017). URL http://dx.doi.org/10.1038/s41598-017-11039-w.

12. Davies, D. & Davies, J. Thermally-driven mantle plumes reconcile multiple hot-spot observations. *Earth and Planetary Science Letters* **278**, 50 – 54 (2009). URL http://www.sciencedirect.com/science/article/pii/S0012821X08007383.

13. Allègre, C. J. Chemical geodynamics. *Tectonophysics* **81**, 109 – 132 (1982). URL http://www.sciencedirect.com/science/article/pii/0040195182901251. Geophysics final symposium.

14. White, W. M. Sources of oceanic basalts: Radiogenic isotopic evidence. *Geology* **13**, 115–118 (1985). URL https://doi.org/10.1130/0091-7613(1985)13<115:SOOBRI>2.0.CO;2. https://pubs.geoscienceworld.org/geology/article-pdf/13/2/115/3507682/i0091-7613-13-2-115.pdf.

15. Allègre, C. J. & Turcotte, D. L. Implications of a two-component marble-cake mantle. *Nature* **323**, 123–127 (1986). URL http://dx.doi.org/10.1038/323123a0.

16. Carlson, R. W. Mechanisms of earth differentiation: Consequences for the chemical structure of the mantle. *Reviews of Geophysics* **32**, 337 (1994). URL http://dx.doi.org/10.1029/94RG01874.

17. Tackley, P. J. Mantle convection and plate tectonics: Toward an integrated physical and chemical theory. *Science* **288**, 2002–2007 (2000). URL http://dx.doi.org/10.1126/science.288.5473.2002.

18. Tackley, P. Mantle geochemical geodynamics. *Treatise on Geophysics* 437–505 (2007). URL http://dx.doi.org/10.1016/B978-044452748-6.00124-3.

19. Gonnermann, H. M. & Mukhopadhyay, S. Non-equilibrium degassing and a primordial source for helium in ocean-island volcanism. *Nature* **449**, 1037–1040 (2007). URL http://dx.doi.org/10.1038/nature06240.

20. Gonnermann, H. M. & Mukhopadhyay, S. Preserving noble gases in a convecting mantle. *Nature* **459**, 560–563 (2009). URL http://dx.doi.org/10.1038/nature08018.

21. Jackson, M. G. *et al.* Helium and lead isotopes reveal the geochemical geometry of the samoan plume. *Nature* **514**, 355–358 (2014). URL http://dx.doi.org/10.1038/nature13794.

22. White, W. Probing the earth's deep interior through geochemistry. *Geochemical Perspectives* 95–251 (2015). URL http://dx.doi.org/10.7185/geochempersp.4.2.

23. Weis, D., Garcia, M. O., Rhodes, J. M., Jellinek, M. & Scoates, J. S. Role of the deep mantle in generating the compositional asymmetry of the hawaiian mantle plume. *Nature Geoscience* **4**, 831–838 (2011). URL http://dx.doi.org/10.1038/ngeo1328.

24. Farnetani, C. G., Hofmann, A. W. & Class, C. How double volcanic chains sample geochemical anomalies from the lowermost mantle. *Earth and Planetary Science Letters* **359-360**, 240–247 (2012). URL http://dx.doi.org/10.1016/j.epsl.2012.09.057.

25. Williams, C. D., Li, M., McNamara, A. K., Garnero, E. J. & van Soest, M. C. Episodic entrainment of deep primordial mantle material into ocean island basalts. *Nature Communications* **6** (2015). URL http://dx.doi.org/10.1038/ncomms9937.

26. Ishii, M. Normal-mode and free-air gravity constraints on lateral variations in velocity and density of earth's mantle. *Science* **285**, 1231–1236 (1999). URL http://dx.doi.org/10.1126/science.285.5431.1231.

27. Masters, G. & Gubbins, D. On the resolution of density within the earth. *Physics of the Earth and Planetary Interiors* **140**, 159–167 (2003). URL http://dx.doi.org/10.1016/j.pepi.2003.07.008.

28. Simmons, N. A., Forte, A. M., Boschi, L. & Grand, S. P. Gypsum: A joint tomographic model of mantle density and seismic wave speeds. *Journal of Geophysical Research* **115** (2010). URL http://dx.doi.org/10.1029/2010JB007631.

29. Trampert, J. Probabilistic tomography maps chemical heterogeneities throughout the lower mantle. *Science* **306**, 853–856 (2004). URL http://dx.doi.org/10.1126/science.1101996.

30. Koelemeijer, P. J., Deuss, A. & Trampert, J. Normal mode sensitivity to earth's d layer and topography on the core-mantle boundary: what we can and cannot see. *Geophysical Journal International* **190**, 553–568 (2012). URL http://dx.doi.org/10.1111/j.1365-246X.2012.05499.x.

31. Lau, H. C. P. *et al.* Tidal tomography constrains earth's deep-mantle buoyancy. *Nature* **551**, 321 EP – (2017). URL https://doi.org/10.1038/nature24452.

32. Trampert, J., Vacher, P. & Vlaar, N. Sensitivities of seismic velocities to temperature, pressure and composition in the lower mantle. *Physics of the Earth and Planetary Interiors* **124**, 255

– 267 (2001). URL http://www.sciencedirect.com/science/article/pii/S0031920101002011.

33. Deschamps, F. & Trampert, J. Mantle tomography and its relation to temperature and composition. *Physics of the Earth and Planetary Interiors* **140**, 277 – 291 (2003). URL http://www.sciencedirect.com/science/article/pii/S0031920103001894.

34. Schubert, G., Masters, G., Olson, P. & Tackley, P. Superplumes or plume clusters? *Physics of the Earth and Planetary Interiors* **146**, 147–162 (2004). URL http://dx.doi.org/10.1016/j.pepi.2003.09.025.

35. Steinberger, B. & Torsvik, T. H. A geodynamic model of plumes from the margins of large low shear velocity provinces. *Geochemistry, Geophysics, Geosystems* **13**, n/a–n/a (2012). URL http://dx.doi.org/10.1029/2011GC003808.

36. Hassan, R., Flament, N., Gurnis, M., Bower, D. J. & Müller, D. Provenance of plumes in global convection models. *Geochemistry, Geophysics, Geosystems* **16**, 1465–1489 (2015). URL http://dx.doi.org/10.1002/2015GC005751.

37. Li, M. & Zhong, S. The source location of mantle plumes from 3d spherical models of mantle convection. *Earth and Planetary Science Letters* **478**, 47 – 57 (2017). URL http://www.sciencedirect.com/science/article/pii/S0012821X17304806.

38. Torsvik, T. H., Burke, K., Steinberger, B., Webb, S. J. & Ashwal, L. D. Diamonds sampled by plumes from the core–mantle boundary. *Nature* **466**, 352–355 (2010). URL http://dx.doi.org/10.1038/nature09216.

39. Burke, K. Plate tectonics, the wilson cycle, and mantle plumes: Geodynamics from the top. *Annual Review of Earth and Planetary Sciences* **39**, 1–29 (2011). URL http://dx.doi.org/10.1146/annurev-earth-040809-152521.

40. Matthews, K. J. *et al.* Global plate boundary evolution and kinematics since the late paleozoic. *Global and Planetary Change* **146**, 226 – 250 (2016). URL http://www.sciencedirect.com/science/article/pii/S0921818116302417.

41. Domeier, M. & Torsvik, T. H. Plate tectonics in the late paleozoic. *Geoscience Frontiers* **5**, 303 – 350 (2014). URL http://www.sciencedirect.com/science/article/pii/S1674987114000061.

42. Müller, R. D. *et al.* Ocean basin evolution and global-scale plate reorganization events since pangea breakup. *Annual Review of Earth and Planetary Sciences* **44**, 107–138 (2016). URL https://doi.org/10.1146/annurev-earth-060115-012211.

43. McNamara, A. K. & Zhong, S. Thermochemical structures beneath africa and the pacific ocean. *Nature* **437**, 1136–1139 (2005). URL http://dx.doi.org/10.1038/nature04066.

44. Zhang, N., Zhong, S., Leng, W. & Li, Z.-X. A model for the evolution of the earth's mantle structure since the early paleozoic. *Journal of Geophysical Research* **115** (2010). URL http://dx.doi.org/10.1029/2009JB006896.

45. Bower, D. J., Gurnis, M. & Seton, M. Lower mantle structure from paleogeographically constrained dynamic earth models. *Geochemistry, Geophysics, Geosystems* **14**, 44–63 (2013). URL http://dx.doi.org/10.1029/2012GC004267.

46. Hassan, R., Müller, R. D., Gurnis, M., Williams, S. E. & Flament, N. A rapid burst in hotspot motion through the interaction of tectonics and deep mantle flow. *Nature* **533**, 239–242 (2016). URL http://dx.doi.org/10.1038/nature17422.

47. Flament, N., Williams, S., Müller, R. D., Gurnis, M. & Bower, D. J. Origin and evolution of the deep thermochemical structure beneath eurasia. *Nature Communications* **8**, 14164 (2017). URL http://dx.doi.org/10.1038/ncomms14164.

48. Zhang, N. & Li, Z.-X. Formation of mantle "lone plumes" in the global downwelling zone — a multiscale modelling of subduction-controlled plume generation beneath the south china sea. *Tectonophysics* **723**, 1 – 13 (2018). URL http://www.sciencedirect.com/science/article/pii/S0040195117305000.

49. Heron, P. J. Mantle plumes and mantle dynamics in the wilson cycle. *Geological Society, London, Special Publications* SP470.18 (2018). URL http://dx.doi.org/10.1144/SP470.18.

50. Dannberg, J. & Gassmöller, R. Chemical trends in ocean islands explained by plume–slab interaction. *Proceedings of the National Academy of Sciences* **115**, 4351–4356 (2018). URL http://dx.doi.org/10.1073/pnas.1714125115.

51. Steinberger, B. & Calderwood, A. R. Models of large-scale viscous flow in the earth's mantle with constraints from mineral physics and surface observations. *Geophysical Journal International* **167**, 1461–1481 (2006). URL http://dx.doi.org/10.1111/j.1365-246X.2006.03131.x.

52. Connolly, J. A. D. The geodynamic equation of state: What and how. *Geochemistry, Geophysics, Geosystems* **10**, n/a–n/a (2009). URL http://dx.doi.org/10.1029/2009GC002540.

53. Stixrude, L. & Lithgow-Bertelloni, C. Thermodynamics of mantle minerals - ii. phase equilibria. *Geophysical Journal International* **184**, 1180–1213 (2011). URL http://dx.doi.org/10.1111/j.1365-246X.2010.04890.x.

54. Xu, W., Lithgow-Bertelloni, C., Stixrude, L. & Ritsema, J. The effect of bulk composition and temperature on mantle seismic structure. *Earth and Planetary Science Letters* **275**, 70–79 (2008). URL http://dx.doi.org/10.1016/j.epsl.2008.08.012.

55. Ni, S., Tan, E., Gurnis, M. & Helmberger, D. Sharp sides to the african superplume. *Science* **296**, 1850–1852 (2002). URL https://science.sciencemag.org/content/296/5574/1850. https://science.sciencemag.org/content/296/5574/1850.full.pdf.

56. Seton, M. *et al.* Global continental and ocean basin reconstructions since 200ma. *Earth-Science Reviews* **113**, 212 – 270 (2012). URL http://www.sciencedirect.com/science/article/pii/S0012825212000311.

57. Torsvik, T. H., Steinberger, B., Cocks, L. R. M. & Burke, K. Longitude: Linking earth's ancient surface to its deep interior. *Earth and Planetary Science Letters* **276**, 273 – 282 (2008). URL http://www.sciencedirect.com/science/article/pii/S0012821X08006328.

58. Kronbichler, M., Heister, T. & Bangerth, W. High accuracy mantle convection simulation through modern numerical methods. *Geophysical Journal International* **191**, 12–29 (2012). URL http://dx.doi.org/10.1111/j.1365-246X.2012.05609.x.

59. Heister, T., Dannberg, J., Gassmöller, R. & Bangerth, W. High accuracy mantle convection simulation through modern numerical methods. II: Realistic models and problems. *Geophysical Journal International* **210**, 833–851 (2017). URL https://doi.org/10.1093/gji/ggx195.

60. Nakagawa, T., Tackley, P. J., Deschamps, F. & Connolly, J. A. D. Incorporating self-consistently calculated mineral physics into thermochemical mantle convection simulations in a 3-d spherical shell and its influence on seismic anomalies in earth's mantle. *Geochemistry, Geophysics, Geosystems* **10**, n/a–n/a (2009). URL http://dx.doi.org/10.1029/2008GC002280.

61. Loken, C. *et al.* Scinet: Lessons learned from building a power-efficient top-20 system and data centre. *Journal of Physics: Conference Series* **256**, 012026 (2010). URL http://dx.doi.org/10.1088/1742-6596/256/1/012026.

62. French, S. W. & Romanowicz, B. A. Whole-mantle radially anisotropic shear velocity structure from spectral-element waveform tomography. *Geophysical Journal International* **199**, 1303–1327 (2014). URL http://dx.doi.org/10.1093/gji/ggu334.

Acknowledgements This publication is part of a project that has received funding from the European Union's Horizon 2020 research and innovation program under the Marie Skłodowska-Curie Grant Agreement 749664 (P. J. Heron). R. N. Pysklywec acknowledges support from a Natural Sciences and Engineering Research Council of Canada Discovery Grant and an allocation with ComputeCanada. J. D. gratefully acknowledges the support of the Deep Carbon Observatory. G.E.S. acknowledges support from the Research Council of Norway through its Centers of Excellence funding scheme, Project Number 223272. J. v. H. acknowledges financial support from NERC (NE/M000281/1). Computations were performed on the Niagara supercomputer at the SciNet HPC Consortium[61]. SciNet is funded by the Canada Foundation for Innovation; the Government of Ontario; Ontario Research Fund-Research Excellence; and the University of Toronto. The authors acknowledge the Texas Advanced Computing Center (TACC, http://www.tacc.utexas.edu) at The University of Texas at Austin for providing high-performance computing resources that have contributed to the research results reported within this paper. We thank the Computational Infrastructure for Geodynamics (geodynamics.org) which is funded by the National Science Foundation under award EAR-0949446 and EAR-1550901 for supporting the development of ASPECT. This paper is part of UNESCO IGCP Project 648: Supercontinent Cycles and Global Geodynamics.

Author contributions. P.J.H. conceived and planned the project; P.J.H. and J.D. coordinated the interpretation of the data and wrote the paper with contributions from G.E.S, R.N.P, J.v.H., and R.G.

Competing Interests. The authors declare that they have no competing financial interests.

Materials & Correspondence. Correspondence and requests for materials should be addressed to P.J.H. (email: philip.j.heron@durham.ac.uk).

S Supporting Information

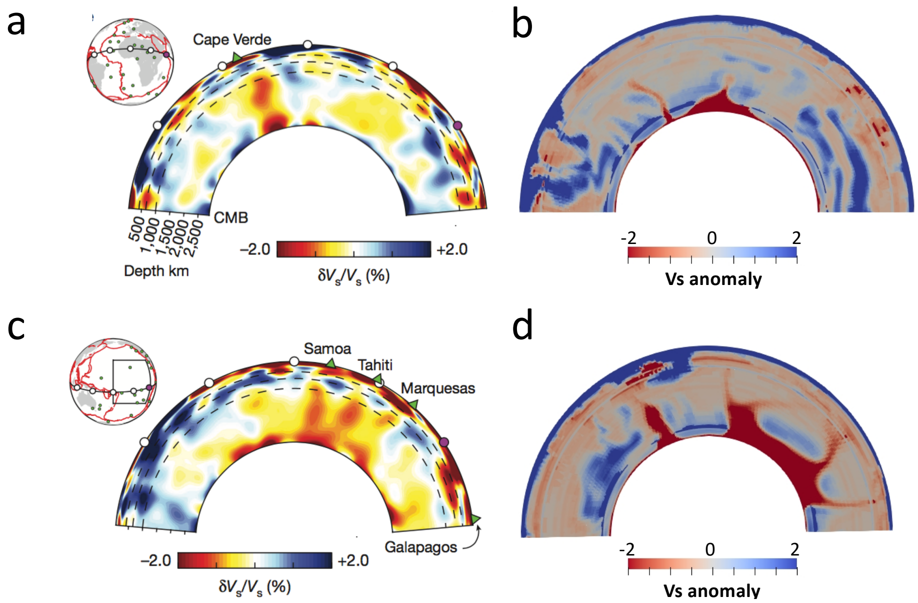

Figure S.1: Whole-mantle depth cross-section modified from[4] of relative shear-velocity variations using model SEMUCB-WM1[62] near Cape Verde (a) and Marquesas (c), with the corresponding shear velocity anomaly output from Model200 shown in (b) and (d), respectively.

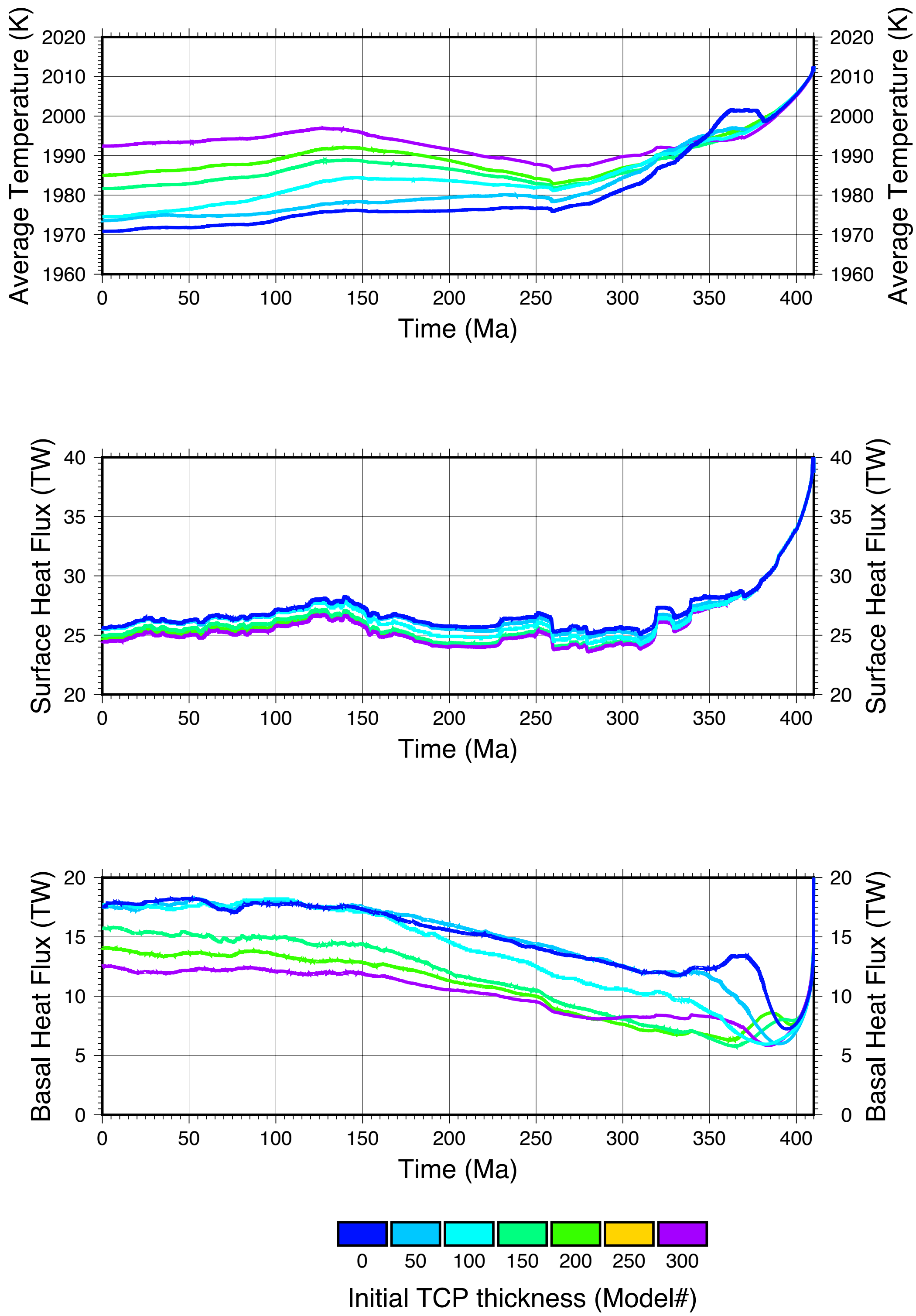

Figure S.2: Thermal evolution of the models. a) Average mantle temperature, b) surface heat flux, c) basal heat flux.

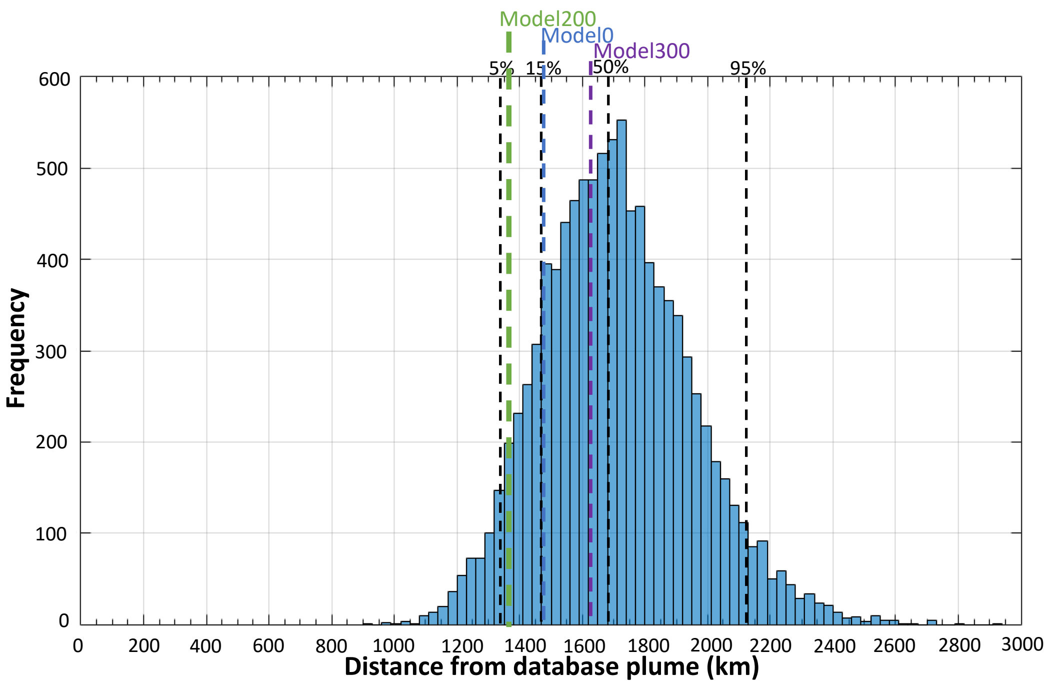

Figure S.3: Model200 performs better than around 95% of the 10,000 random models. Histogram showing the spread of distances from 52% of the database plumes. Annotated are the 5%, 15%, 50%, and 95% distributions of the random models, as well as the Model200, Model0, and Model300 results.

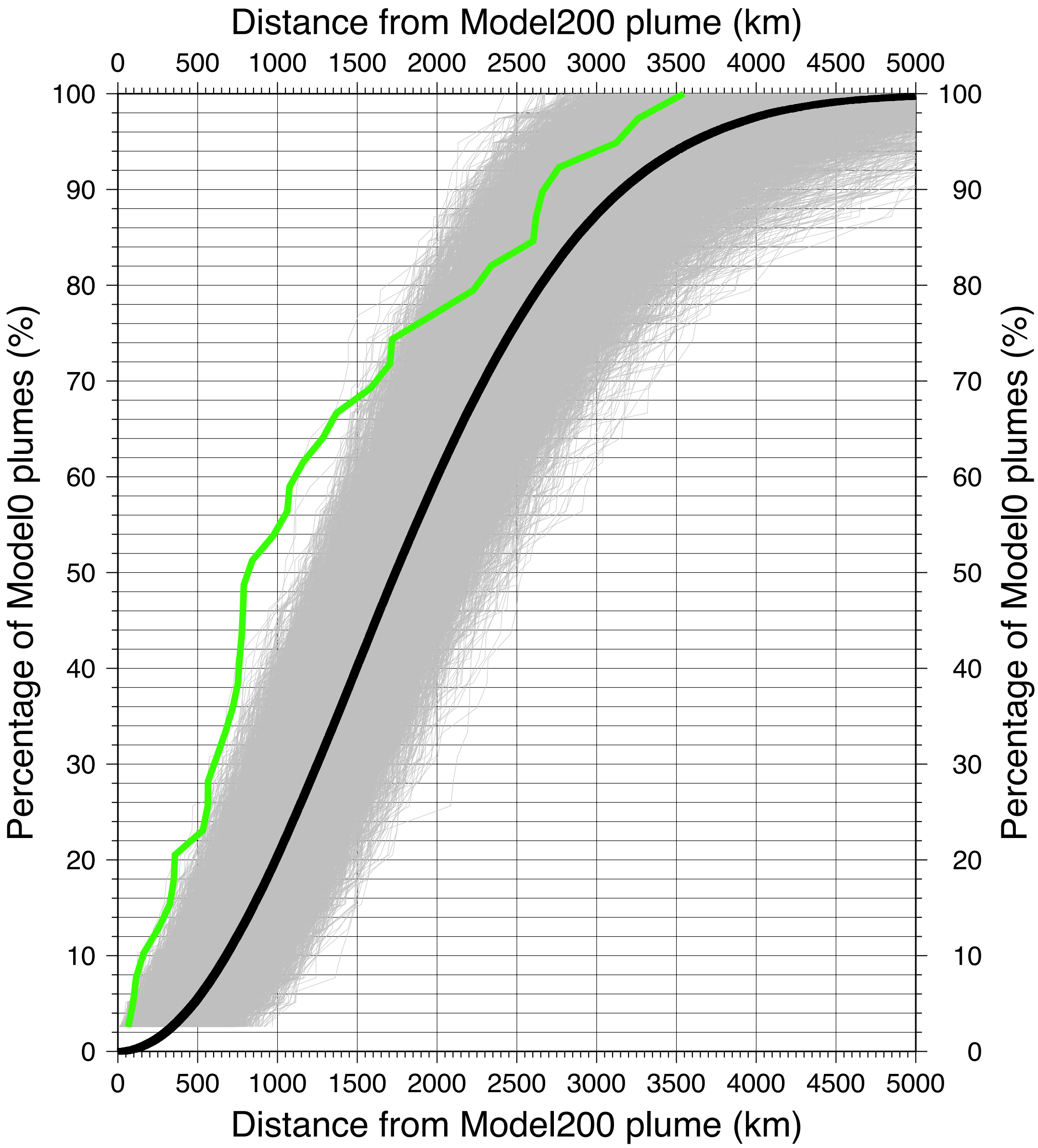

Figure S.4: Analysis of Model0 plume positions at 0 Ma as a function of distance away from nearest Model200 plume. Models have differing number of plumes (see main text). Model0 features no thermo-chemical pile (TCP) and Model200 has a 200 km initial TCP thickness. The black line is the accumulation of 10,000 sets of 39 random plume positions artificially generated (grey lines).

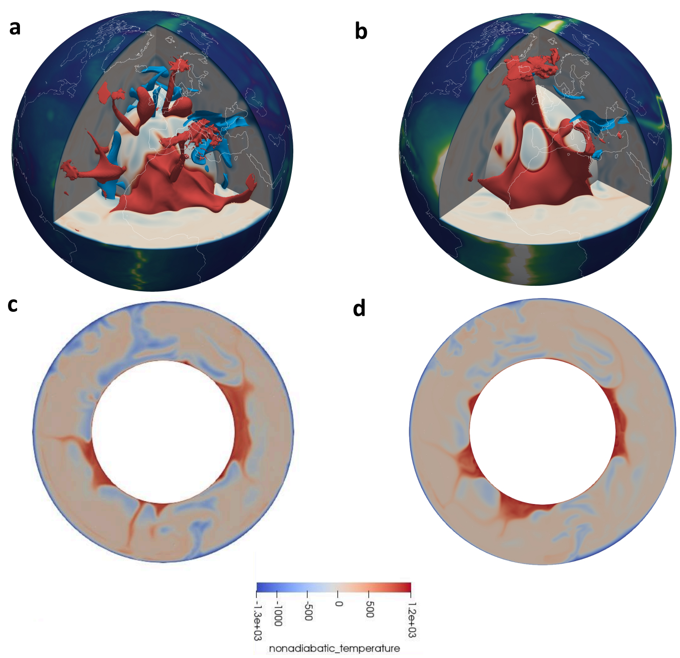

Figure S.5: Comparison between Model200 and Model200hr (a higher resolution simulation). Figure shows a view into the mantle beneath the northern Atlantic and Europe for Model200 (a) and Model200hr (b). Excess temperature anomaly contours are given for warm (300 K, red) and cold (-500 K, blue) regions. Excess temperature at the equator is given for Model200 (c) and Model200hr (d).

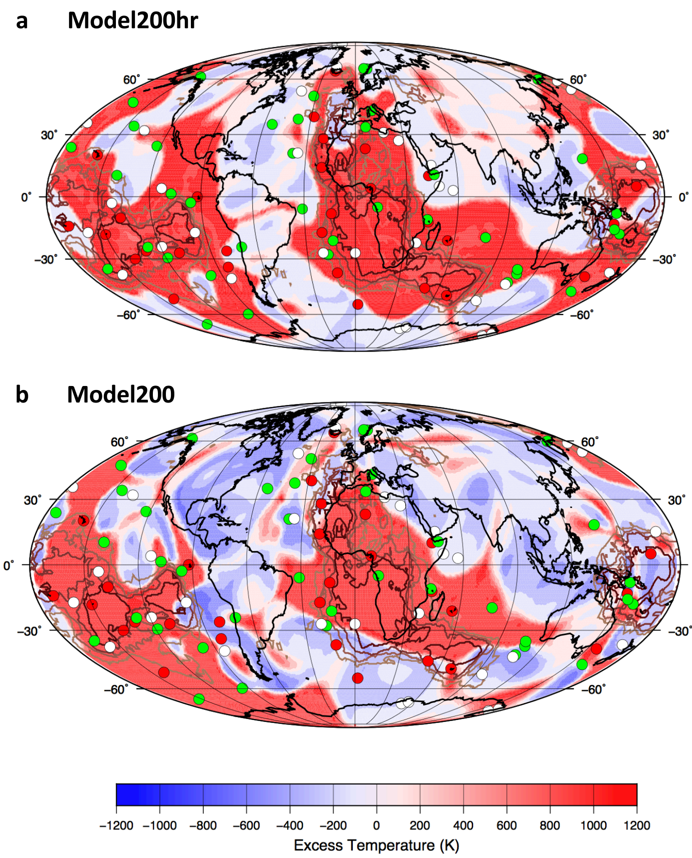

Figure S.6: Comparison between Model200 and Model200hr (a higher resolution simulation). The excess temperature at 2800 km depth for Model200hr is given in (a), with seismic tomography vote contours as Figure 1. Green circles and white circles show Model200 and Model200hr plume positions, respectively. Red circles are of the present-day plume database[1,4]. See Methods for Model200hr description. The excess temperature at 2800 km depth for Model200 is given in (b) for comparison. Circles as (a).

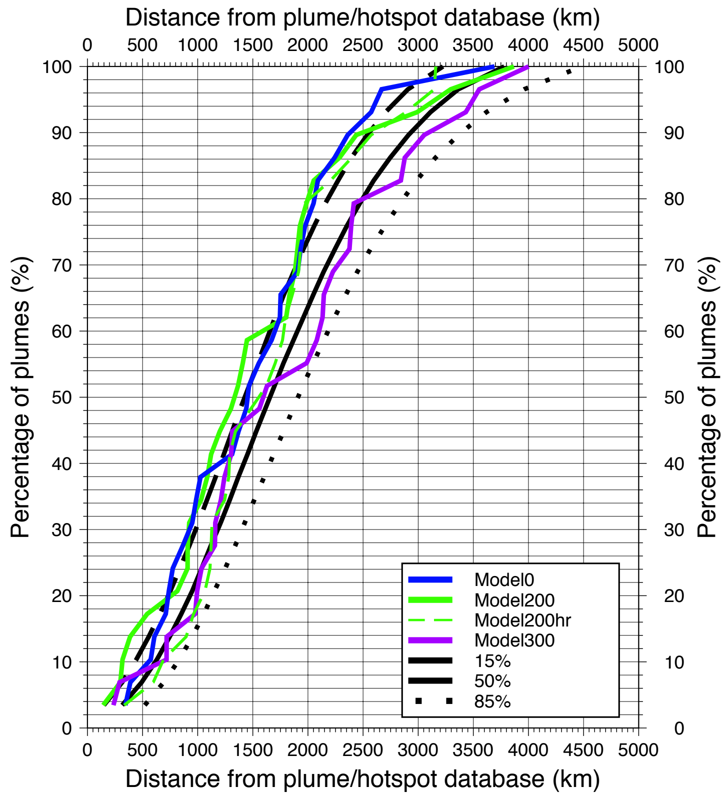

Figure S.7: Analysis of model plume positions at 0 Ma as a function of distance away from nearest present-day plume[1,4]. This image is as Figure 7 (see caption for details) but with the addition of a high resolution Model200 (Model200hr). See Methods for description of high resolution model.

Table S.1: Database of deep plume and hotspot locations[1,4].

#	Latitude	Longitude	Notes
1	-14	-170	Samoa
2	20	-156	Hawaii
3	-18	-150	Tahiti/Society
4	-51	-141	Louisville
5	-30	-140	Macdonald
6	-10	-138	Marquesas
7	-26	-130	Pitcairn
8	-27	-110	Easter
9	0	-92	Galapagos
10	-34	-83	Juan Fernandez
11	-26	-80	San Felix
12	39	-28	Azores
13	28	-20	Mid-Atlantic
14	14	-20	Cape Verde
15	65	-20	Iceland
16	-17	-20	St Helena
17	-8	-14	Ascension
18	-37	-12	Tristan
19	-54	2	Bouvet
20	23	6	Hoggar
21	4	9	Cameroon
22	10	43	Afar
23	-12	43	Comores
24	-45	50	Crozet
25	-21	56	Reunion
26	-49	69	Kerguelen
27	-13	153	Louisade
28	-39	156	Tasmanid
29	5	164	Caroline

Table S.2: List of models with corresponding initial thermo-chemical (TC) thickness, plate reconstruction study, and correlation values. The correlation value is the direct comparison between the African hemisphere slow contour of 8 in the vote map analysis[11] and the outline of the model African thermo-chemical pile. 'Modified' refers to a 410 Myr reconstruction that uses Seton et al.[56] 250 Ma to 90 Ma surface velocities for 410 Ma to 250 Ma, then repeats until present day.

Name	**Initial TC**	**Plate reconstruction**	**Correlation**
Model0	0 km	Matthews et al.[40]	N/A
Model50	50 km	Matthews et al.[40]	N/A
Model100	100 km	Matthews et al.[40]	N/A
Model150	150 km	Matthews et al.[40]	0.71
Model200	200 km	Matthews et al.[40]	0.84
Model250	250 km	Matthews et al.[40]	-
Model300	300 km	Matthews et al.[40]	0.81
Model200s	200 km	Modified Seton et al.[56]	-

Table S.3: Database of large igneous province positions[2,57] from 250 Ma to 100 Ma.

Age (Ma)	**Latitude**	**Longitude**	**LIP name**
251	57.7	54.7	Siberian Traps
200	2.5	341.9	CAMP
182	-44.6	2.8	Karroo Basalts
147	-4	219	Shatsky Rise
145	-26.9	244.3	Megallan Rise
132	-55.3	81.6	Bunbury Basalts
132	-34.9	350.6	Parana-Etendeka
125	-54.7	5.9	Maud Rise
123	-34.5	264.5	Manihiki Plateau
121	38.2	219.7	Ontong Java Plateau
118	-41.6	67	Rajhmahal Traps
114	-52.3	64.9	South Kerguelen
111	-26.4	222	Naura Basalts
100	-45.4	63.3	Central Kerguelen
99	2.6	225.4	Hess Rise